Mitchinson, AJ, Pogson, M, Czanner, G, Conway, D, Wilkinson, RR, Murphy, MF, Siekmann, I and Webb, SD

A stochastic model for topographically influenced cell migration

Highlights

A stochastic model for topographically influenced cell migration

AJ Mitchinson, M Pogson, G Czanner, D Conway, RR Wilkinson, MF Murphy, I Siekmann, SD Webb

- Cell response to surface topography plays a crucial role in physiologic function and biomedical applications.
- Mathematical modelling facilitates the identification of topographic structures promoting certain patterns of cell migration.
- We develop a data-driven stochastic model for topographically influenced cell migration for different topographic patterns.
- Our model shows that migrating cells can be 'guided' by linear topographic patterns, migration speed and trajectory linearity dependent on parallel ridge density.
- Interestingly, adding slight random distortions increases the speed of migration along the linear topographic pattern.

A stochastic model for topographically influenced cell migration

AJ Mitchinson[a,*], M Pogson[b], G Czanner[a,c], D Conway[d], RR Wilkinson[a], MF Murphy[e], I Siekmann[a,c,f,g], SD Webb[h]

[a]*School of Computer Science and Mathematics, Liverpool John Moores University, Liverpool, L3 3AF, United Kingdom*
[b]*Department of Communication and Media, University of Liverpool, Liverpool, L69 7ZG, United Kingdom*
[c]*PROTECT-eHealth, Liverpool John Moores University, Liverpool, L3 3AF, United Kingdom*
[d]*School of Biological Sciences, Queen's University Belfast, Belfast, BT9 5DL, United Kingdom*
[e]*School of Pharmacy and Biomolecular Sciences, Liverpool John Moores University, Liverpool, L3 3AF, United Kingdom*
[f]*Liverpool Centre for Cardiovascular Science, Liverpool, United Kingdom*
[g]*Data Science Research Centre, Liverpool John Moores University, Liverpool, L3 3AF, United Kingdom*
[h]*Syngenta, Crop Protection Research, Jealott's Hill, Bracknell, RG42 6EY, United Kingdom*

Abstract

Migrating cells traverse a range of topographic configurations presented by the native extracellular environment to conduct their physiologic functions. It is well documented cells can modulate their behaviour in response to different topographic features, finding promising applications in biomaterial and bioimplant design. It is useful, in these areas of research, to be able to predict which topographic arrangements could be used to promote certain patterns of migration prior to laboratory experimentation. Despite a profusion of study

*Corresponding author
Email address: ajmitchinsonmath@gmail.com (AJ Mitchinson)

and interest shown in these fields by experimentalists, the related modelling literature is as yet relatively sparse and tend to focus more on either cell-matrix interaction or morphological responses of cells. We propose a mathematical model for individual cell migration based on an Ornstein-Uhlenbeck process, and set out to see if the model can be used to predict migration patterns on 2-d isotropic and anisotropic topographies, whose characteristics can be broadly described as either uniform flat, uniform linear with variable ridge density or non-uniform disordered with variable feature density. Results suggest the model is capable of producing realistic patterns of migration for flat and linear topographic patterns, with calibrated output closely approximating NIH3T3 fibroblast migration behaviour derived from an experimental dataset, in which migration linearity increased with ridge density and average speed was highest at intermediate ridge densities. Exploratory results for non-uniform disordered topographies suggest cell migration patterns may adopt disorderedness present in the topography and that 'distortion' introduced to linear topographic patterns may not impede linear guidance of migration, given it's magnitude is bounded within certain limits. We conclude that an Ornstein-Uhlenbeck based model for topographically influenced migration may be useful to predict patterns of migration behaviour for certain isotropic (flat) and anisotropic (linear) topographies in the NIH3T3 fibroblast cell line, but additional investigation is required to predict with confidence migration patterns for non-uniform disordered topographic arrangements.
Keywords: cell migration, topography, Ornstein-Uhlenbeck, mathematical model, tissue engineering, bioimplant

1. Introduction

Surface topography has long been known to affect cell behaviour. Zoologist R.G. Harrison discovered early in the twentieth century that frog cells would align, elongate and migrate along the silk threads of spider web when presented on a cover slide, suggesting cells were able to both sense and respond to the structural characteristics of their environment [1].

Cells are exposed to a diverse range of topographic arrangements within the complex extracellular environment navigated during migration within the body, existing across different length scales [2, 3, 4]. Experimentally, many cell types have been found to modulate their migration behaviour in response to certain topographic arrangements, such as linear ridges and grooves reported most significantly in fibroblasts [5, 6, 7], but also epithelial [8], endothelial and smooth muscle cells [9]), lattice patterns [10, 11, 12], pillars [13, 14, 15], pits [16] and curvature [17] (for additional detail see any of the following review papers: [18, 19, 20]). Topographically guided migration has even been shown to influence the progression of crucial physiological processes like dermal wound healing [21, 22], and complex pathophysiologies like breast cancer metastases [23, 24].

Exactly how topographies affect cell behaviour mechanistically is not yet completely understood. A leading theoretical model suggests physical confinement potentially restricts the development of focal adhesions in certain locations on the cell, ultimately redirecting cell orientation and subsequent movement [25, 26].

The use of topographies to influence cell behaviour has found promising application in biomaterial and bioimplant design (e.g. tissue-implant integration

[22, 27, 28] and tissue scaffolds [29, 30, 31]), in which it is useful to know which geometries can be used to promote certain patterns of migration. The task of identifying and classifying these topographies with *in vitro* experimentation can be resource intensive.

Modelling studies which incorporate topographic cues into cell migration models have traditionally focused on cell-matrix interactions, in which migration behaviour and extracellular matrix (ECM) fibril properties are dynamically interdependent. Examples of these types of model include Barocas and Tranquillo's work on migration in tissue equivalents such as collagen gels [32], and those by Dallon, Sherratt and co-authors describing scar tissue formation [33, 34]. More recent studies have focused more specifically on mechanistic and morphological aspects of cell migration behaviour in response to topographies, such as a 3-d discrete force-based 'virtual' cell model proposed by Heydari et al. [35], and Winkler, Aranson and Ziebert's lamellipodia-based individual cell model [36]. In general, it appears there is a relative lack of mathematical and computational models to help experimentalists in the design and development of topographies to influence migration behaviours. A similar observation was expressed by Heydari et al. in their recent modelling study, stating "there are very few methods available for robust and accurate modeling that can predict cell behavior prior to experimental evaluations" [35].

Individual-based cell trajectory models, like those published by Dallon, Sherratt and co-authors [33, 34], are particularly useful for prediction and analysis of potential migration patterns of individual cells. The models published by Dallon and co-authors are however formulated to be realistic under the con-

dition that topography structure is an ECM-like fibrillar matrix, producing unrealistic behaviour for topographies with sparse features.

In this study, we develop a mathematical model for topographically influenced migration that is simple, interpretable, and we show can in principle be used to predict patterns of individual cell migration on 2-d isotropic and anisotropic topographic patterns, whose characteristics can be broadly described as either uniform flat, uniform linear and non-uniform disordered both with varied densities (see *Methods 2.1*). Similar to Dallon and co-authors, we use a discrete-point approach that incorporates directional cues from an underlying gradient field representing the arrangement of physical gradients of a topography. Our modelling approach differs in that we assume the discrete point cell migrates according to an Ornstein-Uhlenbeck process in the absence of physical gradients, whose movement is influenced by the presence of such gradients; a similar approach was used by Stokes, Lauffenburger and Williams to describe chemotaxis in endothelial cells [37].

We focus at first on movement on highly structured topographies which have parallel linear features, using published data (see: [7]) of NIH3T3 fibroblast migration on linearly ridged surfaces to calibrate the model (for model calibration see *Results 3.1* and for the calibrated migration model with uniform linear topographic patterns *Results 3.3*); preliminary results for another dataset comprising polished metal surfaces [38] were previously presented by Conway [39]. We then explore how migration might change when linear topographic features are gradually distorted, inspired by fabrication noise present when coarse methods have been used to generate the topographic pattern, producing non-uniform disordered topographic features (see *Results 3.4*).

2. Methods

2.1. Model

The model is based on an Ornstein-Uhlenbeck (OU) cell migration model, used in previous works as a general model of 2-d random motility [40] and as a model for endothelial chemotaxis [37]. This model assumes that given no environmental stimuli or guidance cue cell movement is well approximated by Brownian movement, using a combination of force terms to describe the velocity-time evolution of a single cell.

To account for the influence of some underlying topography, we introduce directional bias into the model. We assume cells tend to avoid steep physical gradients in their migrations and instead reorient toward contour directions. The biased OU model for change in 2-d cell velocity $\boldsymbol{v}(t)$ with respect to time t, is given by Eq. (1).

$$d\boldsymbol{v}(t) = \Big(\kappa\boldsymbol{\varphi}(t) - \beta\boldsymbol{v}(t)\Big)dt + \sqrt{\alpha}d\boldsymbol{W}(t), \tag{1}$$

where κ controls topographic bias, β resistance to motion, α random acceleration and $\boldsymbol{W}(t)$ is the 2-d vector Wiener process. The topographic bias, $\boldsymbol{\varphi}(t)$, is defined by Eq. (2).

$$\boldsymbol{\varphi}(t) = \langle \boldsymbol{g}, \boldsymbol{v} \rangle \frac{\boldsymbol{g}^{\perp}}{\parallel \boldsymbol{g}^{\perp} \parallel}, \tag{2}$$

where $\boldsymbol{g} = \boldsymbol{\nabla} S(x_1, y_1)$, such that $\boldsymbol{\nabla} \equiv \left(\frac{\partial}{\partial x}, \frac{\partial}{\partial y}\right)$, continuous scalar field $S(x, y)$ represents a 2-d surface topography, (x_1, y_1) denotes cell position (assumed to be the centroid of cell surface area) at time t on S, and $\boldsymbol{g}^{\perp}$ is the

orthogonal complement to $\boldsymbol{g}$. The basic components of the topographic bias are illustrated schematically in Figure 1.

Subsequent integrations of Eq. (1) yields displacements over time t for an individual point cell, given by Eq. (3).

$$\boldsymbol{r}(t) = \int_0^t \boldsymbol{v}(t')dt', \tag{3}$$

where, $\boldsymbol{r}(t)$ is the 2-d cell position at time t.

To estimate model parameters, $P = (\alpha, \beta, \kappa) \in \mathbb{R}^3_+$, we use a grid search optimisation method (see *Supplementary material 1.1* for methodological detail). We define an objective function as the nondimensional error function ϵ which, for a given parameter set, e.g. $P_{1,1,1} = (\alpha_1, \beta_1, \kappa_1)$, is calculated by Eq. (4).

$$\epsilon = \sum_{i=1}^{N} \frac{(\zeta_i - \zeta_i^*)^2}{(\zeta_i^*)^2}, \tag{4}$$

where ζ_i is the ith metric derived from model simulations and ζ_i^* is the ith metric derived from experimental data. N is total number of metrics.

For our fitting procedure we use two metrics ($N = 2$): orientation angle θ (°) and migration speed s (μm/h); taking the standard deviation θ_σ and mean s_μ of 100 cell trajectories.

Experimental metric data we use is extracted from a study published by Kim et al. [7]. To make the calculation in Eq. (4), we use population standard deviation of "polarisation angle", $\theta_\sigma^*(°)$, and mean migration speed, s_μ^* (μm/h), over time on an anisotropic substratum with parallel linear ridges spaced in increasing 100 nm increments from densely to sparsely spaced ridges (from 1μm to 9.1μm; see *Supplementary material 1.2* for further study details). We

use this data to find parameter values for the model in relation to surfaces with linear features with either dense, intermediate or sparse ridge densities.

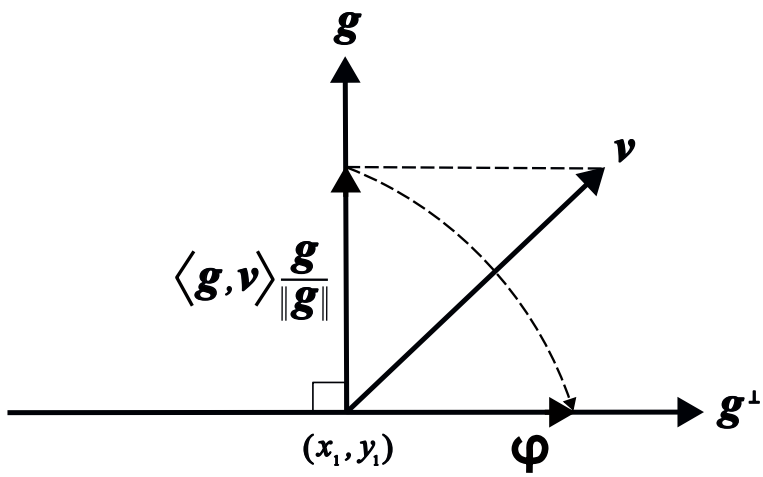

Figure 1: Schematic diagram to illustrate the basic components of topographic bias for the model in relation to cell position at time t, (x_1, y_1). The vector $\boldsymbol{g} = \boldsymbol{\nabla} S(x_1, y_1)$ denotes the steepest local gradient at the point (x_1, y_1) on continuous 2-d surface $S(x, y)$. Orthogonal projection of cell velocity $\boldsymbol{v}$ onto $\boldsymbol{g}$ yields the scalar product, $\langle \boldsymbol{g}, \boldsymbol{v} \rangle$, the associated vector in the direction of $\boldsymbol{g}$ is $\langle \boldsymbol{g}, \boldsymbol{v} \rangle \dfrac{\boldsymbol{g}}{\| \boldsymbol{g} \|^2}$. The orthogonal complement of $\boldsymbol{g}$ is denoted by $\boldsymbol{g}^{\perp}$, where $\langle \boldsymbol{g}, \boldsymbol{g}^{\perp} \rangle = 0$, the bias term being $\boldsymbol{\varphi} = \langle \boldsymbol{g}, \boldsymbol{v} \rangle \dfrac{\boldsymbol{g}^{\perp}}{\| \boldsymbol{g}^{\perp} \|}$.

2.2. Migration metrics

(i) **Orientation angle**. Defined as the argument between cell velocity direction $\boldsymbol{v}$ and fixed axis direction $\boldsymbol{L} = [0, 1]$, the direction of linear features on the topographic patterns used in the study, measured from the discrete point cell position (x_1, y_1) at time t, termed 'orientation angle', $\theta(^\circ)$. The calculation is symmetric about directions orthogonal to $\boldsymbol{L}$ and we determine the positions of the reference angle 0° to be at both opposing linear directions $\boldsymbol{L}$ and $-\boldsymbol{L}$. We measure θ with positive angles clockwise from $\boldsymbol{L}$ and $-\boldsymbol{L}$, keeping the angle range acute, $-90^\circ \leq \theta \leq 90^\circ$ (additional details of the calculation and a schematic diagram of the measurement can be found in *Supplementary material 1.3*).

We compute θ between numerical time increments, j and $j+1$, for every increment and each cell i in a given simulation, to give a distribution of 'orientation angles' for the whole simulation, $\theta_{ij,j+1}$, where $i = 1, ..., N_c$ and $j = 1, ..., N_t - 1$, from which we then calculate the mean, θ_μ, and standard deviation, θ_σ, given by Eq. (5) and Eq. (6) respectively.

$$\theta_\mu = \frac{1}{N_c(N_t - 1)} \sum_{i=1}^{N_c} \sum_{j=1}^{N_t - 1} \theta_{ij,j+1}, \tag{5}$$

where i is the ith cell and j is the jth increment. N_c is total number of cells and N_t is total number of increments.

$$\theta_\sigma = \sqrt{\frac{1}{N_c(N_t - 1)} \sum_{i=1}^{N_c} \sum_{j=1}^{N_t - 1} (\theta_{ij,j+1} - \theta_\mu)^2}. \tag{6}$$

(ii) **Migration speed**. We compute migration speed s (μm/h) from individual cell displacements as with orientation angles, between increments j and $j+1$ for every increment for each cell i in a given simulation, to give a distribution of migration speeds, $s_{ij,j+1}$, from which we calculate the mean migration speed, s_μ, Eq. (7).

$$s_\mu = \frac{1}{N_c(N_t-1)} \sum_{i=1}^{N_c} \sum_{j=1}^{N_t-1} s_{ij,j+1}. \tag{7}$$

Metrics are calculated from multiple simulations of the same stochastic model, Eq. (1), each trajectory taken as representative of the migration behaviour of an individual cell on a sparsely populated substrate.

2.3. Numerical implementation

The software environment we use to generate different topographic patterns and solve the model is MathWorks MATLAB 2021a. To approximate topographic patterns similar to those used to produce the experimental dataset, we generate matrices with data values corresponding to 'depth' values, spatially distributed to approximate the arrangements of uniform linear ridges spaced at different densities, corresponding to 1μm ridges at uniform depth spaced at either high (2μm), intermediate (6μm) or low (9μm) density. For predictions, we introduce random perturbations to these linear arrangements orthogonal to the orientation of the features using a MATLAB pseudo-random number generator, controlling the magnitude of random perturbations with parameter ρ (further details of the methods used to generate topographic patterns for the study can be found in *Supplementary material 1.4*).

We use MATLAB's numerical gradient function to compute an approximate gradient field for each topography, this is then used during the model simulation to influence cell orientation and re-orientation.

We solve the model using an Euler-Maruyama scheme [41] to obtain an approximation for cell migration velocities, obtaining subsequent cell positions by numerical integration. We run repeat model simulations to compute the metrics detailed in *Methods 2.2*.

3. Results

3.1. Parameter estimation

To estimate model parameters we use a grid search optimisation method (see *Supplementary material 1.1* for further detail). We show in Figure 2 a subset of results from the optimisation. Results show error surfaces (as contour plots, for the error ϵ, Eq. (4), over model kinesis parameters β and α) illustrating minima locations (blue) for (a) flat topography at $\kappa = 0$ (the choice of κ here is arbitrary, since there are no surface gradients and the topographic bias exerts no influence on movement) and (b)-(d) 9μm, 6μm and 2μm spaced linear topographies at fixed κ values; (b) $\kappa = 1$, (c) $\kappa = 0.75$ and (d) $\kappa = 0.5$.

We see clearly in Figure 2 (a) parameters are non-identifiable for the flat topography. To approximate parameter combinations for (a), we fit a model polynomial function (blue line) through minima (for further details see *Supplementary 2.1*). By contrast, in Figure 2 (b)-(d), we see clearly identifiable parameter combinations for β and α at given κ values for each of the linear topographic patterns. We find each κ by iterative search through ϵ error surfaces, $E(\alpha, \beta)$, across κ (see *Supplementary material 2.1* for estimation of κ). We then estimate parameter combinations for (b)-(d) by choosing α at an arbitrary minimum for median β over the constrained region of minima, β_η (for further details see *Supplementary 2.1*).

Approximated parameter combinations for the model are given in Table 1 and used to generate model migration trajectories from which $\theta_\sigma(^\circ)$ and $s_\mu(\mu\text{m/h})$ in Figure 3 are calculated, and presented on the same axes as those derived from [7], $\theta^*_\sigma(^\circ)$ and $s^*_\mu(\mu\text{m/h})$.

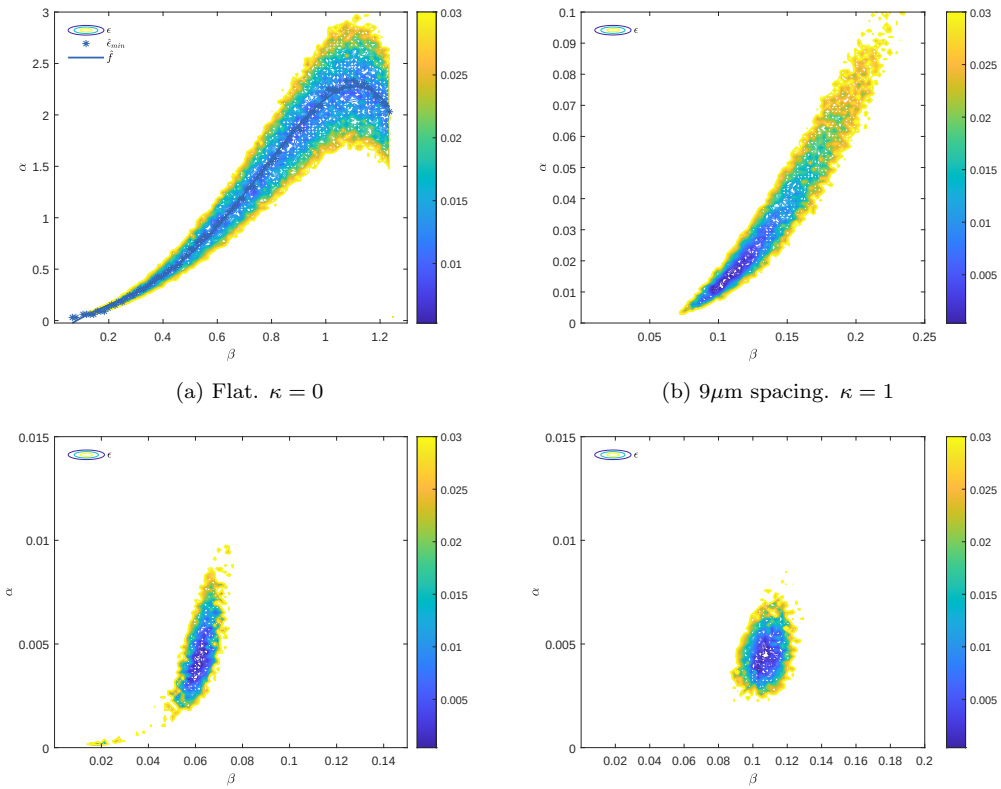

(a) Flat. $\kappa = 0$

(b) 9μm spacing. $\kappa = 1$

(c) 6μm spacing. $\kappa = 0.75$

(d) 2μm spacing. $\kappa = 0.5$

Figure 2: Contour plots showing error ϵ against model kinesis parameters β and α and at fixed values for model bias parameter κ resulting from grid search optimisation for four different topographies: (a) flat, (b) sparse linear (9μm spacing), (c) intermediate linear (6μm spacing) and (d) dense linear (2μm spacing). Colour bar represents ϵ. Blue asterisk denotes approximate minimum values for ϵ, $\hat{\epsilon}_{min}$ (see *Supplementary 2.1* for details of approximation). Blue line is a polynomial function $f(\hat{\beta})$ fit to the set of points $\hat{\epsilon}_{min}$ (see *Supplementary 2.1* for definition). Note that in (a) flat: α and β are non-identifiable, and the relationship is approximately quartic, and in (b)-(d) 9μm, 6μm and 2μm: α and β are identifiable with uncertainty for a given κ. Changes to κ do not influence ϵ for (a), however there is a range for κ for which different and equally valid (under the condition ϵ is small) parameter spaces exist for (b)-(d), such that the choice of κ may be arbitrary within each range. (a) flat: $\kappa = 0$. (b) 9μm: $\kappa = 1$. (c) 6μm: $\kappa = 0.75$. (d) 2μm: $\kappa = 0.5$. Spatial domain: $1000 \times 1000\mu\text{m}^2$. Simulation parameters: $m = 100$, number of cells, $N_c = 100$, time, $t = 540$ minutes, $N_t = 36$ increments, $X_{init} = (500\mu\text{m},500\mu\text{m})$ is the fixed initial position.

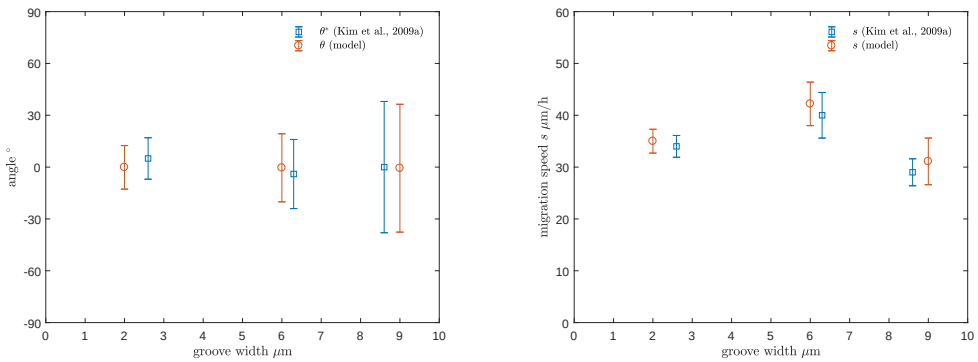

(a) Polarisation and orientation angles θ^* and θ.

(b) Migration speed s^* and s.

Figure 3: Metric data derived from Kim et al. [7] (blue) and the calibrated model (orange) for topographies with average linear groove widths 2.6μm, 6.3μm and 8.6μm and uniform linear groove widths 2μm, 6μm and 9μm, respectively. (a) polarisation angle $\theta^*(^\circ)$ from [7] (square marker: mean, θ^*_μ, error bar: $\theta^*_\mu \pm \theta^*_\sigma$) and orientation angle $\theta(^\circ)$ from the calibrated model (circular marker: mean, θ_μ, error bar: $\theta_\mu \pm \theta_\sigma$), where θ^*_σ and θ_σ denote respective standard deviations. (b) migration speed $s^*(\mu\text{m/h})$ from [7] (square marker: mean, s^*_μ, error bar: $s^*_\mu \pm s^*_{\sigma M}$) and $s(\mu\text{m/h})$ from the calibrated model (circular marker: mean, s_μ, error bar: $s_\mu \pm s_\sigma$), where $s^*_{\sigma M}$ and s_σ denote standard error and standard deviation, respectively. Spatial domain: $1000 \times 1000\mu\text{m}^2$. Migration parameters: $\beta = 0.1$, $\alpha = 0.013$, $\kappa = 1$ (9μm spacing); $\beta = 0.06$, $\alpha = 0.004$, $\kappa = 0.75$ (6μm spacing); $\beta = 0.11$, $\alpha = 0.005$, $\kappa = 0.5$ (2μm spacing). Simulation parameters: $N_c = 100$ cell paths, $t = 540$ minutes, $N_t = 36$ increments, $X_{init} = (500\mu\text{m},500\mu\text{m})$ is the fixed initial position.

Topography	β	α	κ
Flat (no gradient)	0.650	1.068	0.000
Linear 9μm spacing	0.100	0.013	1.000
Linear 6μm spacing	0.060	0.004	0.750
Linear 2μm spacing	0.110	0.005	0.500

Table 1: Migration model parameter combinations (to 3 d.p.) for flat and linearly arranged (with 9μm, 6μm and 2μm spacings, respectively) topographies, determined by grid search optimisation using migration data extracted from [7], and methods outlined in *Supplementary material 1.1* and *2.1*.

3.2. Initial conditions

We use optimisation output detailed in *Results 3.1* to set model migration parameters for simulations using each topography for the following sections (*Results 3.3* and *3.4*), specified in Table 1. We continue to use Table 1 to calibrate the model when we introduce distortion to linear topographies in *Results 3.4*.

Prior to numerical simulations, we fix the initial spatial position of all migration trajectories constant (central on the domain). We see in Table 2 dimensions of the spatial domains, initial positions and units used to generate output for *Results 3.3* and *3.4*. Table 2 also details the number of cell trajectories in simulations, N_c, fixed to aid clarity in trajectory plots and accompanying metrics, unless otherwise stated.

To match the time-lapse speed measurement in the experimental study [7], we set simulation time for every cell to $t = 540$ minutes split into $N_t = 36$ increments each of 15 minute duration, and set Euler-Maruyama sub-increments a tenth the size. Time parameters are kept constant between all simulations.

Section	Domain	X_{init}	N_c	t (minutes)	N_t
Results 3.3	$1000 \times 1000\mu\text{m}^2$	(500μm,500μm)	100	540	36
Results 3.4	$2000 \times 2000\mu\text{m}^2$	(1000μm,1000μm)	100	540	36

Table 2: Initial conditions used for numerical simulations to generate output for *Results 3.3* and *3.4*. Specified are the dimensions and units of each spatial domain (2-d, μm^2), fixed initial position for migration trajectories, X_{init}, number of simulated cell paths, N_c, time in minutes, t, and number of numerical increments, N_t.

3.3. Calibrated migration model with flat and linear topographic patterns

In Figure 4, we present individual cell migration trajectories over time (multi-colour) for the calibrated model with (a) flat, and (b)-(d) linear topographies, with (b) sparse (9μm), (c) intermediate (6μm) and (d) densely (2μm) spaced linear features.

We see in Figure 4 (a)-(d) a clear trend for trajectories to acquire gradually more linearity and greater topographic alignment once topographic features are introduced from (b) through to (d). In Figure 4 (a) we see trajectories for the flat topography show no clear directional preference, trajectories instead appear directionally random, tortuous and stunted. In Figure 4 (b), trajectories for the sparse (9μm spaced) linear topography show some clear topographic alignment and displace significantly in the vertical directions whilst maintaining discernible stochasticity in local directions explored by each cell. In Figure 4 (c), trajectories for the intermediate (6μm spaced) linear topography show a clear preference to follow topographic feature directions resulting in considerable directional linearity, trajectories tending to diverge around the starting position, and follow topographic features in opposing directions. Trajectory displacement also appears considerably more significant, some approaching the domain boundaries. In Figure 4 (d), we see

trajectories for the dense (2μm spaced) linear topography exhibit the most prominent directional linearity, aligning closely with the topographic feature direction. Overall trajectory displacement appears significant but less than for the intermediate (6μm spaced) linear topography.

General trends we see in migration trajectory behaviour are reflected in metrics orientation angle, $\theta(^\circ)$, and migration speed, s (μm/h), for the cell paths over time for each of the topographies, shown as cumulative distributions for each topography in Figure 5 (left and right columns, respectively). Statistical data for the distributions are represented by red dashes, their corresponding values listed in Table 3 and Table 4, respectively.

Descending the left column of Figure 5, we clearly see both the shape and spread of distributions for θ change distinctively across topographies with increasing feature density, (a)-(g). The shape of distributions evolves from approximately uniform for the flat topography (a) to bell-shaped, approximately symmetric around the linear feature direction (0°), for the linear topographies (c)-(g). This appears to support earlier observations that model migration trajectories simulated for the flat topography show no apparent directional preference, whilst trajectories for the linear topographies show topographic alignment. Table 3 (right column) shows how the density of linear topographic features affect topographic alignment. The orientation angle standard deviation, θ_σ, reduces markedly with each increase to linear topographic feature density, also apparent in Figure 5 (left column) where the spread of distributions reduce the more densely packed with linear features the topographies become from (c)-(g) (light red dash is θ_σ).

We see different trends in distributions for migration speed, s (μm/h), in Fig-

ure 5 (right column), which clearly change both in shape and in the location of their centre in s. The shape of these distributions evolve from right-skewed for the flat topography (b) to approximately bell-shaped for the densest linear topography (h). Notably, we also see the distribution centre shift in s for (b)-(h), indicating each topography has a different effect on migration speed. Statistics for these distributions in Table 4 show explicitly these trends for mean and median speed s_μ and s_η, respectively, and first and third quartiles s_{Q_1} and s_{Q_3}, respectively. In Table 4, we notice that the intermediate (6μm spaced) linear topography, corresponding to Figure 5 (f), appears to encourage the highest migration speeds, including highest mean, s_μ, median, s_η, and quartiles s_{Q_1} and s_{Q_3} out of all topographies presented. It is also apparent from Table 4 there may exist a small range of linear spacings for which migration speed may be maximised, for which evidently a 9μm spacing is too sparse and a 2μm spacing too dense.

The trend we observe between linear feature density and migration speed s is also reflected in the mean-squared displacement over time of migration trajectories (see Appendix A).

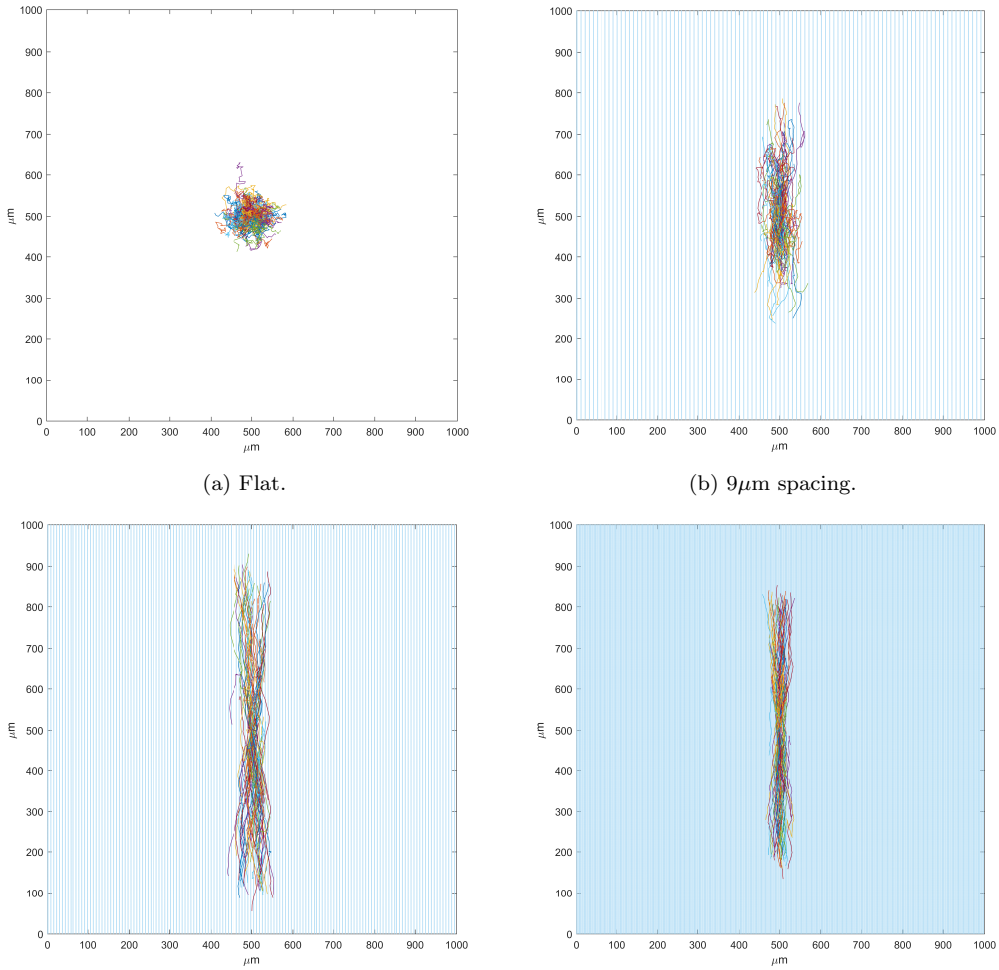

(a) Flat.

(b) 9μm spacing.

(c) 6μm spacing.

(d) 2μm spacing.

Figure 4: Calibrated model migration trajectories over time (multi-colour) over gradient fields (blue) of four different topographies: (a) flat (no gradient), (b) 9μm linear spacings, (c) 6μm linear spacings and (d) 2μm linear spacings, (b)-(d) with constant ridge width 1μm and depth 0.4μm. Trajectories develop a clear linearity when introduced to the linearly arranged topographies, the extent of linearity present dependent on the feature density. There is a clear trend for trajectories to show more pronounced linearity with increasing linear feature density (b)-(d). Spatial domain: $1000 \times 1000\mu\text{m}^2$. Migration parameters: (a) $\beta = 0.65$, $\alpha = 1.07$, $\kappa = 0$, (b) $\beta = 0.1$, $\alpha = 0.013$, $\kappa = 1$, (c) $\beta = 0.06$, $\alpha = 0.004$, $\kappa = 0.75$, (d) $\beta = 0.11$, $\alpha = 0.005$, $\kappa = 0.5$. Simulation parameters: $N_c = 100$ cell paths, $t = 540$ minutes, $N_t = 36$ increments, $X_{init} = (500\mu\text{m},500\mu\text{m})$ is the fixed initial position.

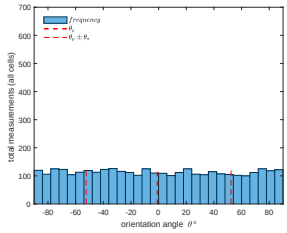

(a) Flat. $\theta(^\circ)$.

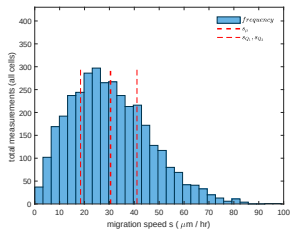

(b) Flat. s (μm/h).

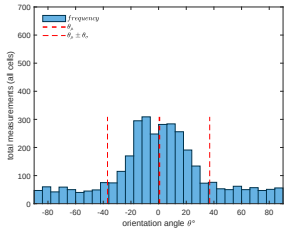

(c) 9μm spacing. $\theta(^\circ)$.

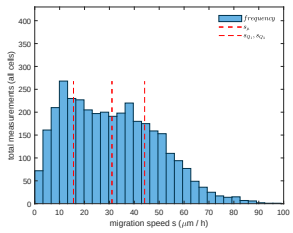

(d) 9μm spacing. s (μm/h).

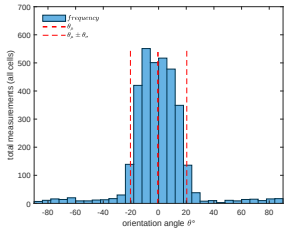

(e) 6μm spacing. $\theta(^\circ)$.

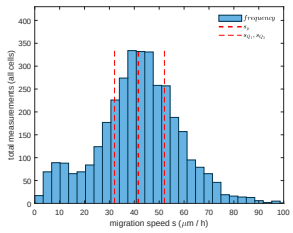

(f) 6μm spacing. s (μm/h).

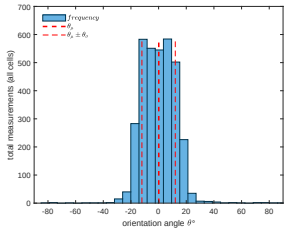

(g) 2μm spacing. $\theta(^\circ)$.

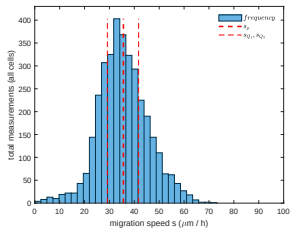

(h) 2μm spacing. s (μm/h).

Figure 5: Orientation angle, $\theta(^\circ)$, (left column) and migration speed, s (μm/h), (right column) cumulative distributions for the four different topographies (rows): (a)-(b) flat, (c)-(d) 9μm spacing, (e)-(f) 6μm spacing and (g)-(h) 2μm spacing. Distributions for both $\theta(^\circ)$ and s (μm/h) display total measurements taken for all cells at $N_t = 36$ increments over $t = 540$ minutes simulation time (for details see *Methods 2.2*). Distributions for θ (left column) are approximately uniform for the flat topography (a), acquiring a symmetric bell-shape for the linear topographies (c)-(g), standard deviation, θ_σ, (red, light) dependent on feature density. Distributions for s (right column) are right-skewed for flat (b) and sparse linear topographies (d), changing to an approximate bell-shape with denser linear topographies (f)-(h). Simulations produce maximal average speed, s_μ, (red, heavy) for the 6μm linearly spaced topography, (f).

Topography	$\theta_\mu(^\circ)$	$\theta_\sigma(^\circ)$
Flat (no gradient)	-0.79	52.4
Linear 9μm spacing	0.61	37.0
Linear 6μm spacing	-0.48	20.4
Linear 2μm spacing	0.12	12.1

Table 3: Orientation angle $\theta(^\circ)$ distribution statistics (to 3 s.f.), mean, θ_μ, and standard deviation, θ_σ, (columns) for each topography presented in Figures 4 and 5: flat, sparse linear (9μm spacing), intermediate linear (6μm spacing) and dense linear (2μm spacing) (rows).

Topography	$s_\mu(\mu\text{m/h})$	$s_\eta(\mu\text{m/h})$	$s_{Q_1}(\mu\text{m/h})$	$s_{Q_3}(\mu\text{m/h})$
Flat (no gradient)	30.4	28.8	18.4	41.1
Linear 9μm spacing	31.0	29.3	15.6	44.1
Linear 6μm spacing	41.6	42.4	32.1	52.1
Linear 2μm spacing	35.6	34.9	29.2	41.7

Table 4: Migration speed $s(\mu\text{m/h})$ distribution statistics (to 3 s.f.), mean, s_μ, median, s_η, first and third quartiles respectively, s_{Q_1} and s_{Q_3}, (columns) for each topography presented in Figures 4 and 5: flat, sparse linear (9μm spacing), intermediate linear (6μm spacing) and dense linear (2μm spacing) (rows).

3.4. Model predictions with randomly perturbed linear topographic patterns

In the following section we present model migration trajectory (Figure 6 - 8) and metric (Figure 9, Appendix B contains additional information) output for linear topographies with dense, intermediate and sparse topographic features which have been gradually perturbed with random noise, or 'distorted', using the methods described in *Methods 2.3* and *Supplementary material 1.4* (where ρ is a perturbation or 'distortion' parameter for surface features).

In Figure 6, for the set of topographies with dense (2μm spaced) (a) linear and (b)-(d) randomly perturbed linear features, we see a clear reduction in trajectory linearity as surface distortion is introduced across topographies (a)-(d). Trajectories appear to mirror the 'disorderedness' in the topographies, becoming more tortuous and randomly or unpredictably directional with increasing surface distortion. In Figure 6 (d), trajectories still appear to maintain a perceptible degree of general alignment with the prevailing topographic feature direction, however alignment fades once surface distortion degrades remaining linear characteristics of the topography (observations made in results not shown). Trajectories also extend noticeably further on the domain as surface distortion increases, indicating potential changes to migration speed.

In Figure 7, for the set of topographies with intermediate (6μm spaced) (a) linear and (b)-(d) randomly perturbed linear features, we see a similar pattern, a reduction in trajectory linearity and increased disorderedness with surface distortion (a)-(d), which is more gradual. Thus, we see in (a)-(d) general alignment with the prevailing feature direction (vertical axis), which

similarly fades when the surface is sufficiently randomly arranged. Notably, trajectories extend much further, up to domain boundaries (d), with increased surface distortion.

In Figure 8, for the set of topographies with sparse (9μm spaced) (a) linear features and (b)-(d) randomly perturbed linear features, we see the familiar general trend repeat, reduction in trajectory linearity with increasing surface distortion (a)-(d), but here trajectories align much more weakly to the prevailing direction of topographic features (d). Trajectories also, whilst appearing to extend with increasing surface distortion, appear comparatively stunted to topographies with denser spacings, indicating a less significant effect on migration speed.

In Figure 9 (a)-(b), for the dense (2μm spaced) topographies shown in Figure 6, we see clear trends for both accompanying (a) orientation angle, $\theta(^\circ)$, and (b) migration speed, s (μm/h), distribution statistics through increasing ρ. In Figure 9 (a), we see mean orientation angle, θ_μ, remain centred around 0°, whilst standard deviation, θ_σ, represented by error bars, broadens significantly through ρ, supporting earlier observations that trajectories lose linearity as the surface is gradually distorted. In Appendix B, we see in Figure B.11 (left column), distribution shape for the more linearly organised topographies, (a) and (c), appears bell-shaped but, with increase to ρ, evolves bimodal characteristics, (e) and (g). In Figure 9 (b), we see both median migration speed, s_η (μm/h), and first and third quartiles, s_{Q_1} and s_{Q_3}, represented by error bars, increase significantly through ρ. The third quartile, s_{Q_3}, remains significantly larger than the first quartile, s_{Q_1}. In Appendix B, we see in Figure B.11 (right column), distribution shape is uni-modal and

right-skewed for lower ρ, (b) and (d), and acquire slightly more symmetry with increasing ρ, (f) and (h). Also evident is the marked shift in s with increasing ρ, accompanied by a clear monotonic increase in mean migration speed, s_μ.

In Figure 9 (c)-(d), for the intermediate (6μm spaced) topographies shown in Figure 7, we see trends for both accompanying (c) orientation angle, $\theta(^\circ)$, and (d) migration speed, s (μm/h), distribution statistics which are similar to but distinct from those observed for the dense (2μm) spaced topographies through increasing ρ. In Figure 9 (c), we see θ_σ evidently broaden but comparatively moderately through ρ. In Appendix B, we see in Figure B.12 (left column), distribution shape clearly also begins to shift from bell-shaped for the more linearly organised topographies, (a) and (c), to bimodal with increasing ρ, though less acutely. In Figure 9 (d), we see a pronounced increase in median migration speed, s_η, first and third quartiles, s_{Q_1} and s_{Q_3}, through ρ, continuing to grow beyond $\rho = 1$ rather than saturate. In Appendix B, we see in Figure B.12 (right column), distribution shape is similarly uni-modal and right-skewed for lower ρ, (b) and (d), becoming more symmetrical with increasing ρ, (f) and (h), whilst remaining asymmetrical.

In Figure 9 (e)-(f), for the sparse (9μm spaced) topographies shown in Figure 8, we see subtler trends for both accompanying (e) orientation angle, $\theta(^\circ)$, and (f) migration speed, s (μm/h), distribution statistics, following a more distinct pattern through increasing ρ. In Figure 9 (e), we see θ_σ barely broaden through ρ, remaining only weakly directed by the prevailing feature direction. In Appendix B, we see in Figure B.13 (left column), the distribution shape remains bell-shaped with increasing ρ but flattens significantly, approaching

uniform-like characteristics for the more disordered topographies. In Figure 9 (f), we see comparatively minor increase to median migration speed, s_η and first and third quartiles, s_{Q_1} and s_{Q_3}, through ρ, continuing to grow beyond $\rho = 1$. In Appendix B, we see in Figure B.13 (right column), distribution shape, like that for θ, remains largely stable with increasing ρ, uni-modal and right-skewed (b)-(h), though with steadily broadening quartiles and a small monotonic increase to s_μ.

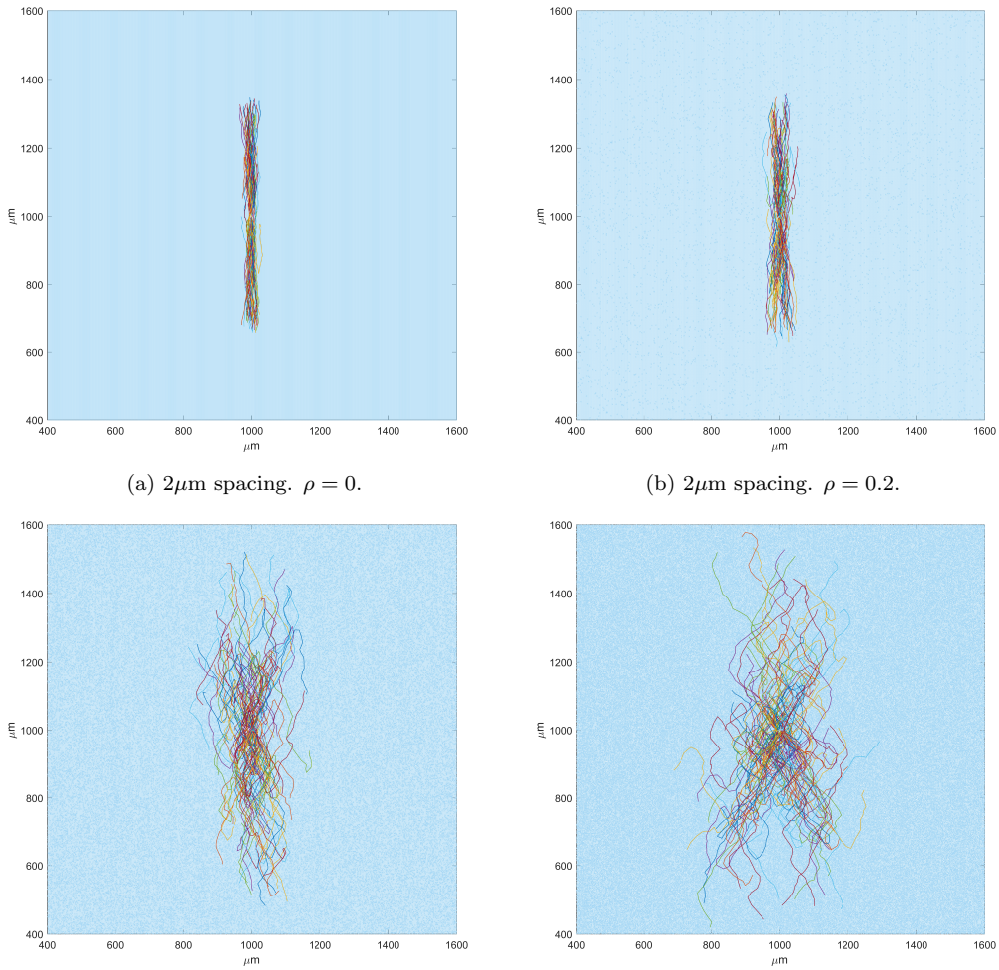

(a) 2μm spacing. $\rho = 0$.

(b) 2μm spacing. $\rho = 0.2$.

(c) 2μm spacing. $\rho = 0.35$.

(d) 2μm spacing. $\rho = 0.5$.

Figure 6: Model migration trajectories (multi-colour) over gradient fields (blue) of four topographies with linear 2μm groove and 1μm ridge width topographic features perturbed stochastically in the direction orthogonal to the ridge/groove plane with four different 'noise' levels, determined by feature perturbation parameter ρ (see *Supplementary material 1.4*): (a) $\rho = 0$ (linear), (b) $\rho = 0.2$, (c) $\rho = 0.35$ and (d) $\rho = 0.5$. Trajectories begin to lose directional linearity with the introduction of feature perturbation, the degree of directional unpredictability dependent on ρ (increasing with ρ). Spatial domain: $2000 \times 2000\mu\text{m}^2$. Depth: 0.4μm. Migration parameters: (a)-(d) $\beta = 0.11$, $\alpha = 0.005$, $\kappa = 0.5$. Simulation parameters: (a)-(d) $N_c = 100$ cell paths, $t = 540$ minutes, $N_t = 36$ increments, $X_{init} = (1000\mu\text{m},1000\mu\text{m})$ is the fixed initial position.

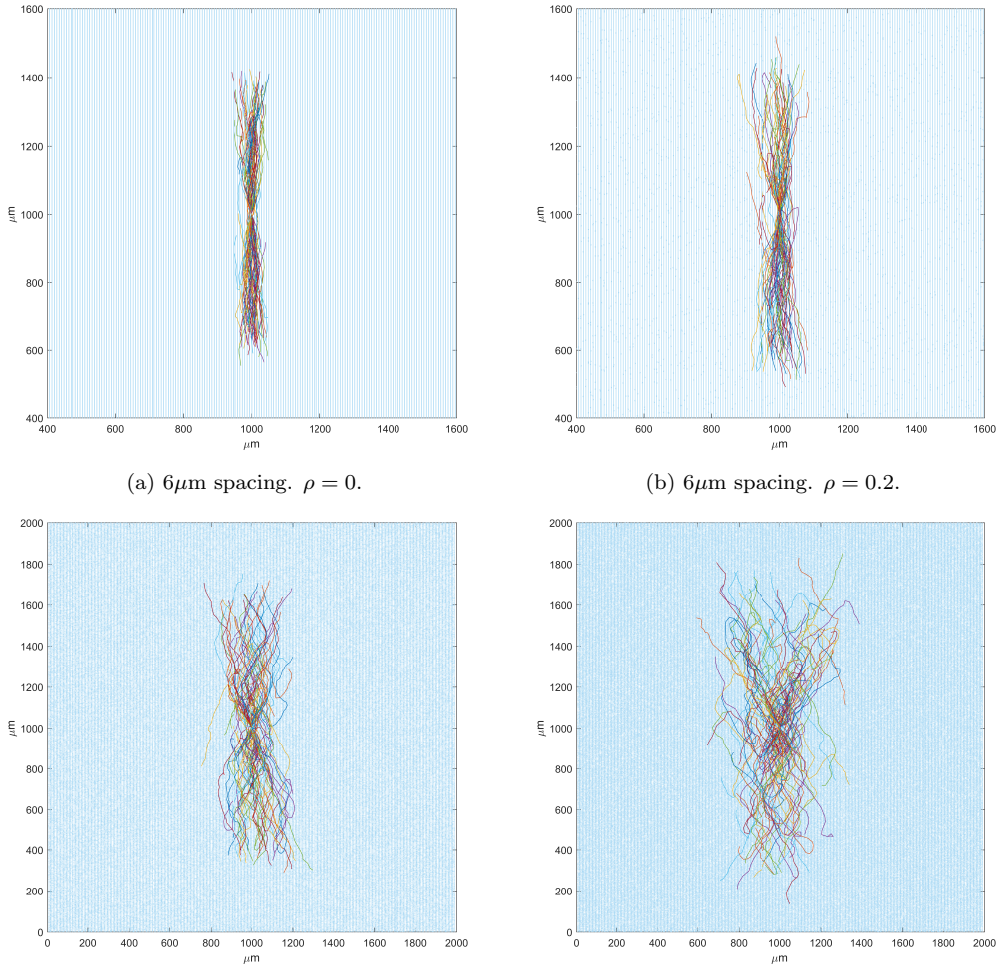

(a) 6μm spacing. $\rho = 0$.

(b) 6μm spacing. $\rho = 0.2$.

(c) 6μm spacing. $\rho = 0.35$.

(d) 6μm spacing. $\rho = 0.5$.

Figure 7: Model migration trajectories (multi-colour) over gradient fields (blue) of four topographies with linear 6μm groove and 1μm ridge width topographic features, perturbed in the manner described in *Supplementary material 1.4* using four different 'noise' levels determined by feature perturbation parameter ρ: (a) $\rho = 0$, (b) $\rho = 0.2$, (c) $\rho = 0.35$ and (d) $\rho = 0.5$. Similar to Figure 6, trajectories clearly lose directional linearity with the introduction of feature perturbation, the degree of directional unpredictability also dependent on ρ (similarly, increasing with ρ). Notably, trajectories show much more significant dispersal as ρ is increased; see (d). Spatial domain: $2000 \times 2000\mu\text{m}^2$. Depth: 0.4$\mu$m. Migration parameters: (a)-(d) $\beta = 0.06$, $\alpha = 0.004$, $\kappa = 0.75$. Simulation parameters: (a)-(d) $N_c = 100$ cell paths, $t = 540$ minutes, $N_t = 36$ increments, $X_{init} = (1000\mu\text{m},1000\mu\text{m})$ is the fixed initial position.

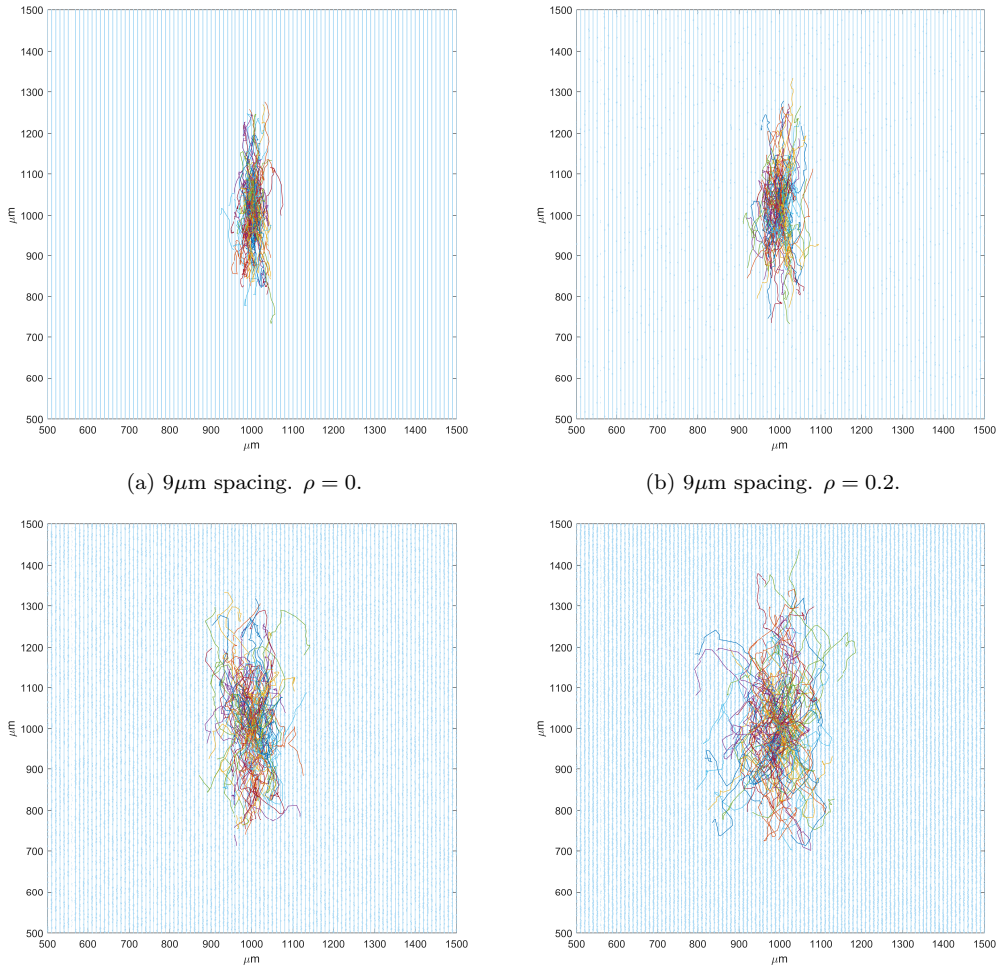

(a) 9μm spacing. $\rho = 0$.

(b) 9μm spacing. $\rho = 0.2$.

(c) 9μm spacing. $\rho = 0.35$.

(d) 9μm spacing. $\rho = 0.5$.

Figure 8: Model migration trajectories (multi-colour) over gradient fields (blue) of four topographies with linear 9μm groove and 1μm ridge width topographic features, perturbed in the manner described using four different 'noise' levels determined by feature perturbation parameter ρ: (a) $\rho = 0$, (b) $\rho = 0.2$, (c) $\rho = 0.35$ and (d) $\rho = 0.5$. Trajectories clearly become more directionally random with the introduction of feature perturbation, the degree also dependent on ρ (similarly, increase to ρ). Spatial domain: $2000 \times 2000\mu\text{m}^2$. Depth: 0.4$\mu$m. Migration parameters: (a)-(d) $\beta = 0.1$, $\alpha = 0.013$, $\kappa = 1$. Simulation parameters: (a)-(d) $N_c = 100$ cell paths, $t = 540$ minutes, $N_t = 36$ increments, $X_{init} = (1000\mu\text{m},1000\mu\text{m})$ is the fixed initial position.

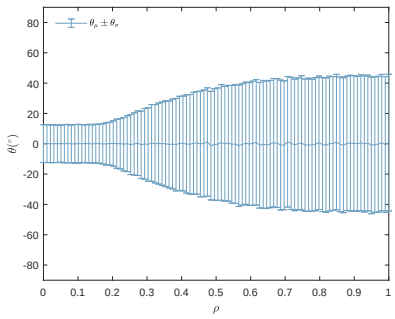

(a) 2μm. $\theta(^\circ)$ vs ρ.

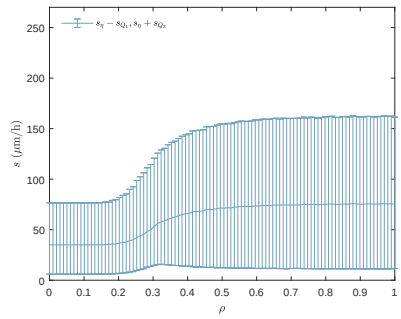

(b) 2μm. s (μm/h) vs ρ.

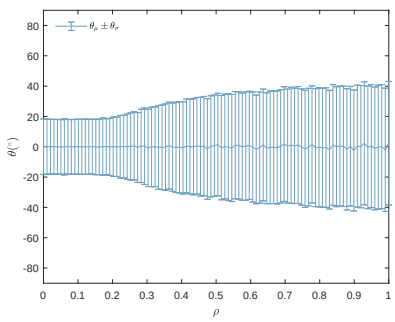

(c) 6μm. $\theta(^\circ)$ vs ρ.

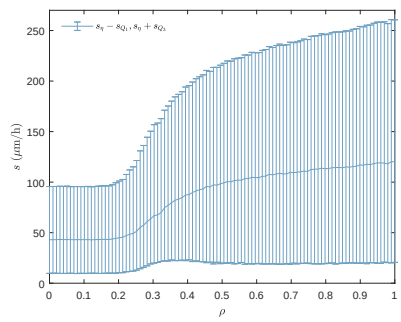

(d) 6μm. s (μm/h) vs ρ.

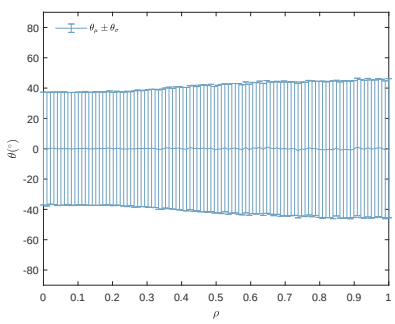

(e) 9μm. $\theta(^\circ)$ vs ρ.

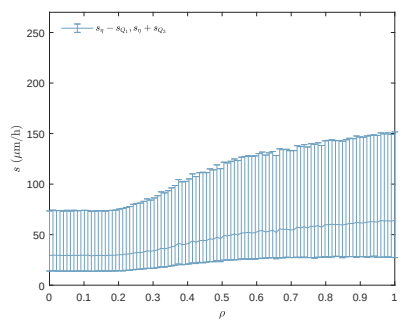

(f) 9μm. s (μm/h) vs ρ.

Figure 9: Orientation angle, $\theta(^\circ)$, (left column) and migration speed, s (μm/h), (right column) distribution statistics against feature perturbation parameter ρ for the three different topographic feature densities (rows): (a)-(b) 2μm spacing, (c)-(d) 6μm spacing, (e)-(f) 9μm spacing. Left column shows mean orientation angle, θ_μ, with standard deviation, θ_σ, represented by error bars ($\theta_\mu \pm \theta_\sigma$). Right column shows median migration speed, s_η, with first and third quartiles, s_{Q_1} and s_{Q_3}, represented by error bars ($s_\eta - s_{Q_1}$, $s_\eta + s_{Q_3}$). Spatial domain: $2000 \times 2000\mu\text{m}^2$. Simulation parameters: $\rho = 0, ..., 1$ in 100 increments, $N_c = 1000$ cell paths, $t = 540$ minutes, $N_t = 36$ increments, $X_{init} = (1000\mu\text{m}, 1000\mu\text{m})$ is the fixed initial position.

4. Discussion

In this study, we proposed a stochastic model for topographically influenced cell migration. The model was based on an Ornstein-Uhlenbeck (OU) process, modified to respond to surface topographic gradients. The introduction of topographic bias was based on the assumption migrating cells would steer away from gradient directions and instead towards contour directions. To calibrate the model, we used experimental data comprising two distinct metrics, polarisation angle, $\theta^*(^\circ)$, and migration speed, $s^*(\mu\text{m/h})$, taken of NIH3T3 fibroblast cell migration trajectory paths for four different topographies with two distinct properties and patterns: one isotropic (flat) and three anisotropic (linear with different ridge spacings) [7]. We used a grid search optimisation method to fit model simulations to this metric data, using estimation methods to approximate parameter values. Calibrated model output comprised sample migration trajectories, and accompanying 'orientation angle', $\theta(^\circ)$, and migration speed, s (μm/h), metric distributions for four topographic patterns designed to mimic those in the study we use to parametrise and calibrate the model [7]: one isotropic topographic pattern (flat, i.e. no surface gradients present) and three anisotropic patterns with uniform linear $1 \times 0.4\mu$m ridge features spaced in the intervals 9μm, 6μm and 2μm, respectively, in a repeating pattern.

Simulations, presented in Figure 4 (a)-(d), showed alignment and linearity of migration was markedly greater when introduced to the linear topographic patterns, clearly increasing with increased ridge density; the most clearly 'aligned' trajectories were observed for the most densely packed linear topography (2μm spacing). This was reflected in distributions for θ in Figure

5 (left column), evolving from approximately uniform for the flat topography (indicating approximately random movement) to bell-shaped when introduced to linear patterns (indicating alignment with the topographic pattern), standard deviation, θ_σ, reducing significantly which each reduction to linear feature spacing. The monotonic decrease in θ_σ (from 9μm to 2μm spacing) in Figure 5 (c)-(g) was similarly reported in the study used to parametrise and calibrate the model [7], as was linearly directional migration at substratum regions of high ridge density (an average spacing of 2.6μm). The intermediately spaced (6μm) linear pattern clearly maximised mean migration speed, s_μ, compared with linear patterns featuring narrower or wider ridge spacings (2μm and 9μm). This trend was also reported in the aforementioned experimental study [7], the highest average migration speed s_μ^* on substratum regions with intermediate ridge densities (an average spacing of 6.3μm).

We then used the calibrated model to predict how migration behaviour might change when linear topographic patterns are gradually distorted, becoming disordered and randomly arranged once distorted with sufficient magnitude. The intention was to explore in a general way how distortion introduced by coarse methods of surface fabrication (e.g. etching or polishing) may affect the trajectories of migrating cells.

Preserving the dimensions used for previous linear topographic patterns (such that there is a sparse, intermediate and dense pattern), we introduce 'noise' in which the linear pattern is randomly perturbed in the plane orthogonal to ridge direction. The 'noise' level is determined by feature perturbation parameter ρ, which is incrementally increased to generate new topographic patterns with increasingly distorted features on which to test the model.

Predictions suggest distortion introduced to uniform linear features induce degradation in linearity and alignment of migration trajectories, dependent on the magnitude of distortion and surface density of the topographic pattern. We found in general that instead, with intensified surface distortion (increase to ρ), cell direction showed increasing deviations from the ridge direction and cell speed increased, this being the case for each variation in surface density of topographic pattern. We see this evident in Figures 6 - 8, where migration trajectories lose directional linearity and topographic alignment with increase to ρ for all linear feature spacings tested, approximately mirroring 'disorderedness' in the arrangement of the topographic pattern. Standard deviation for orientation angle, θ_σ, also clearly increased for all densities of topographic pattern (see Figure 9, left column). We also see in Appendix B distribution shape for θ for the 2μm and 6μm topographic patterns change over the approximate interval $0 \leq \rho \leq 0.5$, from bell-shaped to bimodal, suggesting significant deviations from an orientation angle of $0°$, i.e. the original linear ridge direction, prompted by increased distortion to surface patterns.

Interestingly, predictions also suggest that more randomly arranged topographic features may increase migration speed compared to uniform linear features, evident in distributions for s which shifted markedly in s for all densities of topographic pattern, s_μ increasing monotonically with ρ as the patterns became more disordered (see Appendix B). This is an unexpected result, as one would expect the presence of additional topographic obstacles to present a navigational challenge for migrating cells, and such a finding for disordered topographic patterns is not to our knowledge reported in the

experimental literature (e.g. see [38]). Although it may be possible that linear patterns without distortion constrain cell movement. The introduction of distortion to surface patterns may remove these constraints while still 'guiding' the cells in an approximately linear direction.

Predictions also suggest that 'distortion' introduced to linear topographic patterns may not impede the guidance of migration in a linear direction, given its magnitude is bounded within certain limits; perhaps as far as the general linear characteristics of the pattern are maintained. In Figure 9, there appears to exist a step change in orientation angle θ and speed s around $\rho = 0.2$, suggesting magnitude of distortion introduced at this 'intensity' of perturbation may be significant enough to begin to disrupt movement patterns of the migrating cells. The finding suggests linearly guided topographically influenced migration may exist within precision limits for the topographic features, and that 'approximately linear' features may still suffice to linearly guide migration. It may be interesting to explore further where exactly these limits exist as it may improve both our understanding of cell behaviour and the utility of certain surface processing methods for controlling and regulating it.

Declaration of competing interests

The authors declare that they have no known competing financial interests or personal relationships that could have appeared to influence the work reported in this paper.

Acknowledgements

We would like to acknowledge important discussions about the work with Dr John McKenzie (Strathclyde) and Dr Stewart Chidlow (LJMU), and those with various members of Liverpool John Moores Mathematical Biology Group. A special thanks to the doctoral supervisory team which helped to bring about the study.

Authors' contributions

AJM, SDW, MP, MM and DC conceptualised the study. AJM conducted the study under the supervision of SDW, IS, MP, MM and RRW. MM and GC aided data curation and analysis. AJM wrote the initial draft of the manuscript, which was revised with SDW and IS.

Funding

This research was funded by Liverpool John Moores University Faculty of Engineering and Technology through a doctoral studentship.

Appendix A. Results 3.3: Mean-squared displacement (MSD) over time t for flat and linear topographies

Mean-squared displacement (MSD) over time t for the flat (blue), 9μm (red), 6μm (yellow) and 2μm (purple) linearly spaced topographies are shown in Figure A.10. We see in Figure A.10 a similar trend as in migration speed, MSD over time being highest on the intermediately spaced linear features (6μm, yellow); significantly larger than for the flat topography. The presence of linear topographic features in general appears to increase MSD over time of calibrated model migration trajectories.

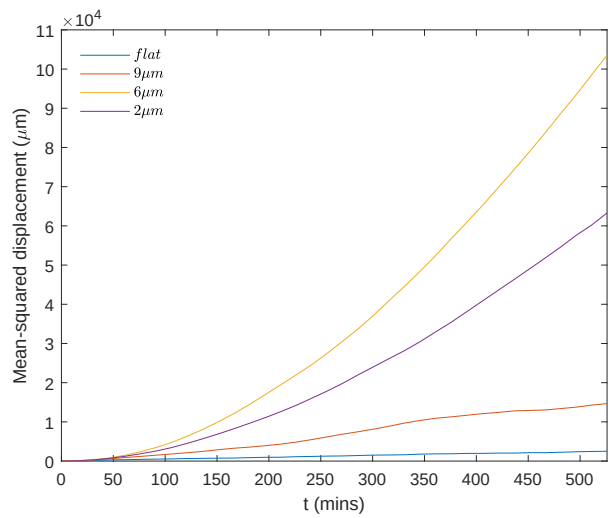

Figure A.10: Mean-squared displacement (MSD) (μm) over time t for flat (blue), 9μm (red), 6μm (yellow) and 2μm (purple) linearly spaced topographies. We see MSD over time t is highest for the 6μm spaced linear features (yellow) compared to the other topographies, markedly greater than for the flat topography (blue). Spatial domain: $1000 \times 1000\mu\text{m}^2$. Migration parameters: (blue) $\beta = 0.65$, $\alpha = 1.07$, $\kappa = 0$, (red) $\beta = 0.1$, $\alpha = 0.013$, $\kappa = 1$, (yellow) $\beta = 0.06$, $\alpha = 0.004$, $\kappa = 0.75$, (purple) $\beta = 0.11$, $\alpha = 0.005$, $\kappa = 0.5$. Simulation parameters: $N_c = 100$ cell paths, $t = 540$ minutes, $N_t = 36$ increments, $X_{init} = (500\mu\text{m},500\mu\text{m})$ is the fixed initial position.

Appendix B. *Results 3.4*: Orientation angle, $\theta(^\circ)$, and migration speed, s (μm/h) distributions and statistics

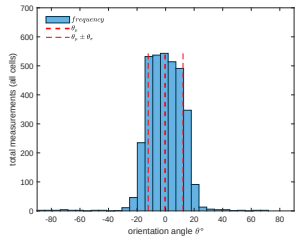

(a) 2μm. $\rho = 0$. $\theta(^\circ)$.

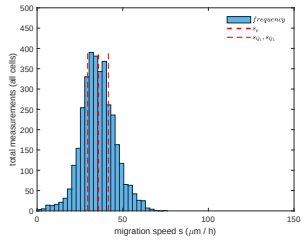

(b) 2μm. $\rho = 0$. s (μm/h).

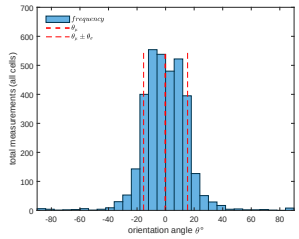

(c) 2μm. $\rho = 0.2$. $\theta(^\circ)$.

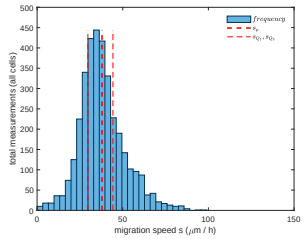

(d) 2μm. $\rho = 0.2$. s (μm/h).

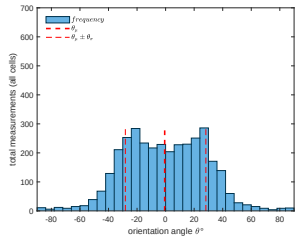

(e) 2μm. $\rho = 0.35$. $\theta(^\circ)$.

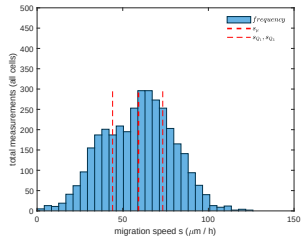

(f) 2μm. $\rho = 0.35$. s (μm/h).

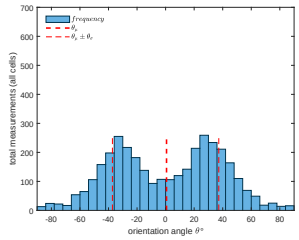

(g) 2μm. $\rho = 0.5$. $\theta(^\circ)$.

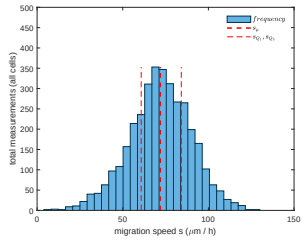

(h) 2μm. $\rho = 0.5$. s (μm/h).

Figure B.11: Orientation angle, $\theta(^\circ)$, and migration speed, s (μm/h), distributions (left and right column, respectively) for the four topographies in Figure 6 (rows): (a)-(h) dense (2μm) spaced linear features; (a)-(b) $\rho = 0$, (c)-(d) $\rho = 0.2$, (e)-(f) $\rho = 0.35$ and (g)-(h) $\rho = 0.5$. We see θ distributions (left column) shift from bell-shaped uni-modal to bimodal with increase to ρ (a)-(g), accompanied by increase to θ_σ (red, light). We see s distributions (right column) shift markedly along the s axis with increase to ρ (b)-(h) and a clear monotonic increase in s_μ (red, heavy) with ρ. Accompanying distribution statistics are listed in Tables B.5 and B.6. Model migration and simulation parameters: see Figure 6.

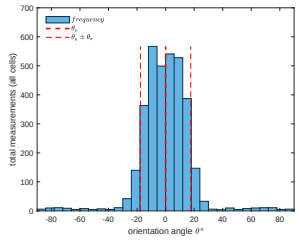

(a) 6μm. $\rho = 0$. $\theta(°)$.

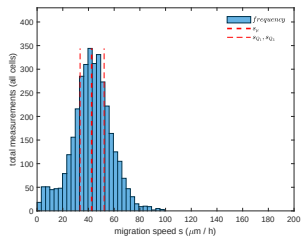

(b) 6μm. $\rho = 0$. s (μm/h).

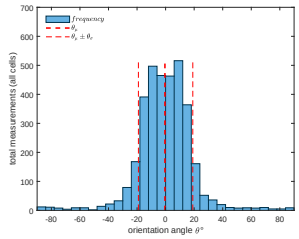

(c) 6μm. $\rho = 0.2$. $\theta(°)$.

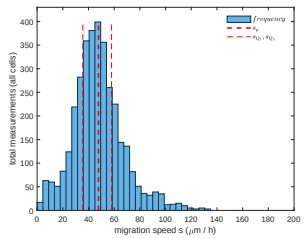

(d) 6μm. $\rho = 0.2$. s (μm/h).

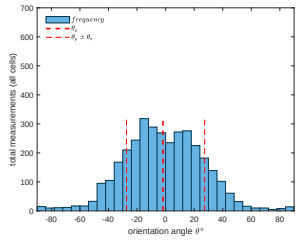

(e) 6μm. $\rho = 0.35$. $\theta(°)$.

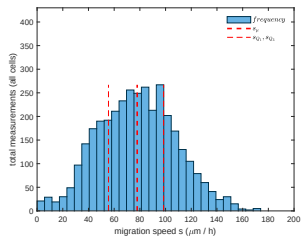

(f) 6μm. $\rho = 0.35$. s (μm/h).

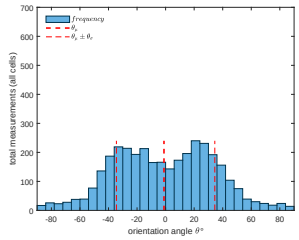

(g) 6μm. $\rho = 0.5$. $\theta(°)$.

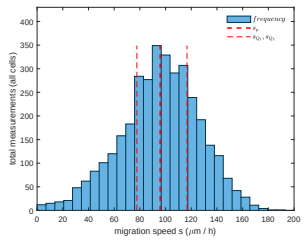

(h) 6μm. $\rho = 0.5$. s (μm/h).

Figure B.12: Orientation angle, $\theta(°)$, and migration speed, s (μm/h), distributions (left and right column, respectively) for the four topographies in Figure 7 (rows): (a)-(h) intermediate (6μm) spaced linear features; (a)-(b) $\rho = 0$, (c)-(d) $\rho = 0.2$, (e)-(f) $\rho = 0.35$ and (g)-(h) $\rho = 0.5$. For θ distributions (left column) we also see a shift in distribution shape from bell-shaped uni-modal to bimodal with increase to ρ, and only a moderate rise in θ_σ(red, light). In s distributions (right column) we see a clear trend for increased distribution symmetry and a surge in s_μ (red, heavy) with increase to ρ. Accompanying distribution statistics are listed in Tables B.7 and B.8. Model migration and simulation parameters: see Figure 7.

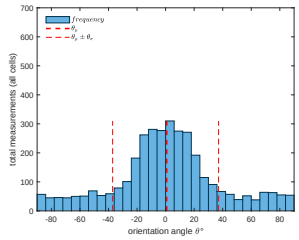

(a) 9μm. $\rho = 0$. $\theta(°)$.

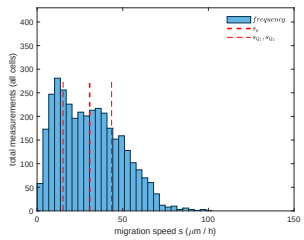

(b) 9μm. $\rho = 0$. s (μm/h).

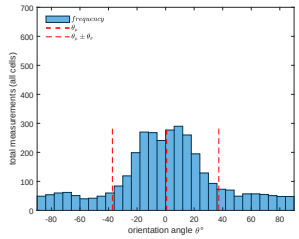

(c) 9μm. $\rho = 0.2$. $\theta(°)$.

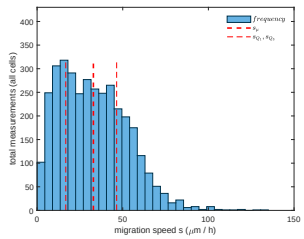

(d) 9μm. $\rho = 0.2$. s (μm/h).

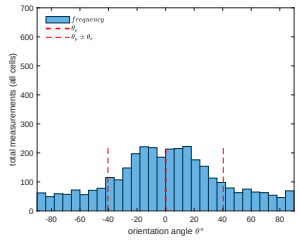

(e) 9μm. $\rho = 0.35$. $\theta(°)$.

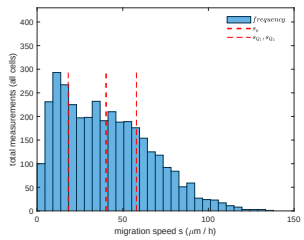

(f) 9μm. $\rho = 0.35$. s (μm/h).

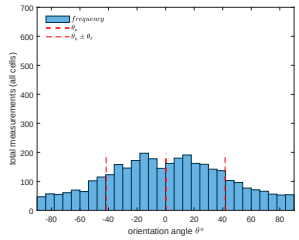

(g) 9μm. $\rho = 0.5$. $\theta(°)$.

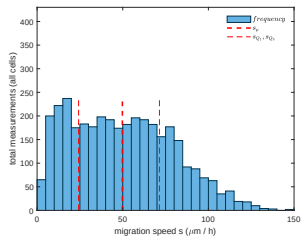

(h) 9μm. $\rho = 0.5$. s (μm/h).

Figure B.13: Orientation angle, $\theta(°)$, and migration speed, s (μm/h), distributions (left and right column, respectively) for the four topographies in Figure 8 (rows): (a)-(h) sparse ($9\mu m$) spaced linear features; (a)-(b) $\rho = 0$, (c)-(d) $\rho = 0.2$, (e)-(f) $\rho = 0.35$ and (g)-(h) $\rho = 0.5$. We see in all θ distributions (left column) a stable bell shape maintained through to $\rho = 0.5$, (g), which flattens and only a small increase to θ_σ (red, light) with increase to ρ. We see s distributions (right column) maintain a consistent positive-skew with broadening quartiles s_{Q_1} and s_{Q_3} (red, light) and a moderate increase in s_μ (red, heavy) with increase to ρ. Accompanying distribution statistics are listed in Tables B.9 and B.10. Model migration and simulation parameters: see Figure 8.

ρ	$\theta_\mu(^\circ)$	$\theta_\sigma(^\circ)$
0	-0.33	12.2
0.2	-0.22	15.4
0.35	-0.64	28.2
0.5	0.65	37.3

Table B.5: Dense (2μm spaced). Orientation angle $\theta(^\circ)$ distribution statistics (to 3 s.f.), mean, θ_μ, and standard deviation, θ_σ, (columns) across variation in distortion parameter ρ for the dense (2μm spaced) topographies (rows), shown in Figures 6 and B.11.

ρ	$s_\mu(\mu\text{m/h})$	$s_\eta(\mu\text{m/h})$	$s_{Q_1}(\mu\text{m/h})$	$s_{Q_3}(\mu\text{m/h})$
0	35.7	35.2	29.5	41.6
0.2	37.9	36.3	29.7	44.3
0.35	59.2	60.4	44.1	73.4
0.5	71.9	72.2	60.8	84.2

Table B.6: Dense (2μm spaced). Migration speed s (μm/h) distribution statistics (to 3 s.f.), mean, s_μ, median, s_η, first and third quartiles respectively, s_{Q_1} and s_{Q_3}, (columns) across variation in distortion parameter ρ for the dense (2μm spaced) topographies (rows), shown in Figures 6 and B.11.

ρ	$\theta_\mu(^\circ)$	$\theta_\sigma(^\circ)$
0	0.01	17.6
0.2	−0.48	19.1
0.35	−1.83	27.4
0.5	−1.14	34.5

Table B.7: Intermediate (6μm spaced). Orientation angle $\theta(^\circ)$ distribution statistics (to 3 s.f.), mean, θ_μ, and standard deviation, θ_σ, (columns) across variation in distortion parameter ρ for the intermediate (6μm spaced) topographies (rows), shown in Figures 7 and B.12.

ρ	$s_\mu(\mu\text{m/h})$	$s_\eta(\mu\text{m/h})$	$s_{Q_1}(\mu\text{m/h})$	$s_{Q_3}(\mu\text{m/h})$
0	42.5	42.8	33.5	52.2
0.2	47.8	46.2	35.6	58.0
0.35	77.9	77.7	55.6	98.5
0.5	95.8	97.1	77.7	116.7

Table B.8: Intermediate (6μm spaced). Migration speed s (μm/h) distribution statistics (to 3 s.f.), mean, s_μ, median, s_η, first and third quartiles respectively, s_{Q_1} and s_{Q_3}, (columns) across variation in distortion parameter ρ for the intermediate (6μm spaced) topographies (rows), shown in Figures 7 and B.12.

ρ	$\theta_\mu(^\circ)$	$\theta_\sigma(^\circ)$
0	0.77	37.1
0.2	0.58	37.3
0.35	0.03	40.4
0.5	0.18	41.7

Table B.9: Sparse (9μm spaced). Orientation angle $\theta(^\circ)$ distribution statistics (to 3 s.f.), mean, θ_μ, and standard deviation, θ_σ, (columns) across variation in distortion parameter ρ for the sparse (9μm spaced) topographies (rows), shown in Figures 8 and B.13.

ρ	$s_\mu(\mu\text{m/h})$	$s_\eta(\mu\text{m/h})$	$s_{Q_1}(\mu\text{m/h})$	$s_{Q_3}(\mu\text{m/h})$
0	30.7	29.0	15.2	43.5
0.2	32.9	31.0	16.7	46.4
0.35	40.3	37.0	18.2	58.0
0.5	49.8	48.1	24.2	71.4

Table B.10: Sparse (9μm spaced). Migration speed s (μm/h) distribution statistics (to 3 s.f.), mean, s_μ, median, s_η, first and third quartiles respectively, s_{Q_1} and s_{Q_3}, (columns) across variation in distortion parameter ρ for the sparse (9μm spaced) topographies (rows), shown in Figures 8 and B.13.

References

[1] R. G. Harrison, The reaction of embryonic cells to solid structures, Journal of Experimental Zoology 17 (4) (1914) 521–544.

[2] A. D. Doyle, R. J. Petrie, M. L. Kutys, K. M. Yamada, Dimensions in cell migration, Current Opinion in Cell Biology 25 (5) (2013) 642–649.

[3] G. Charras, E. Sahai, Physical influences of the extracellular environment on cell migration, Nature Reviews Molecular Cell Biology 15 (12) (2014) 813–824.

[4] I. A. Janson, A. J. Putnam, Extracellular matrix elasticity and topography: Material-based cues that affect cell function via conserved mechanisms, Journal of Biomedical Materials Research Part A 103 (3) (2015) 1246–1258.

[5] J.-P. Kaiser, A. Bruinink, Investigating cell–material interactions by monitoring and analysing cell migration, Journal of Materials Science: Materials in Medicine 15 (4) (2004) 429–435.

[6] A. D. Doyle, F. W. Wang, K. Matsumoto, K. M. Yamada, One-dimensional topography underlies three-dimensional fibrillar cell migration, The Journal of Cell Biology 184 (4) (2009) 481–490.

[7] D.-H. Kim, K. Han, K. Gupta, K. W. Kwon, K.-Y. Suh, A. Levchenko, Mechanosensitivity of fibroblast cell shape and movement to anisotropic substratum topography gradients, Biomaterials 30 (29) (2009) 5433–5444.

[8] B. A. Dalton, X. F. Walboomers, M. Dziegielewski, M. D. Evans, S. Taylor, J. A. Jansen, J. G. Steele, Modulation of epithelial tissue and cell migration by microgrooves, Journal of Biomedical Materials Research: An Official Journal of The Society for Biomaterials, The Japanese Society for Biomaterials, and The Australian Society for Biomaterials and the Korean Society for Biomaterials 56 (2) (2001) 195–207.

[9] S. A. Biela, Y. Su, J. P. Spatz, R. Kemkemer, Different sensitivity of human endothelial cells, smooth muscle cells and fibroblasts to topography in the nano–micro range, Acta Biomaterialia 5 (7) (2009) 2460–2466.

[10] J. Mai, C. Sun, S. Li, X. Zhang, A microfabricated platform probing cytoskeleton dynamics using multidirectional topographical cues, Biomedical Microdevices 9 (4) (2007) 523–531.

[11] D.-H. Kim, C.-H. Seo, K. Han, K. W. Kwon, A. Levchenko, K.-Y. Suh, Guided cell migration on microtextured substrates with variable local density and anisotropy, Advanced Functional Materials 19 (10) (2009) 1579–1586.

[12] H. Jeon, H. Hidai, D. J. Hwang, K. E. Healy, C. P. Grigoropoulos, The effect of micronscale anisotropic cross patterns on fibroblast migration, Biomaterials 31 (15) (2010) 4286–4295.

[13] M. T. Frey, I. Y. Tsai, T. P. Russell, S. K. Hanks, Y.-l. Wang, Cellular responses to substrate topography: role of myosin ii and focal adhesion kinase, Biophysical Journal 90 (10) (2006) 3774–3782.

[14] A. Saez, M. Ghibaudo, A. Buguin, P. Silberzan, B. Ladoux, Rigidity-driven growth and migration of epithelial cells on microstructured anisotropic substrates, Proceedings of the National Academy of Sciences 104 (20) (2007) 8281–8286.

[15] R. D. Sochol, A. T. Higa, R. R. Janairo, S. Li, L. Lin, Unidirectional mechanical cellular stimuli via micropost array gradients, Soft Matter 7 (10) (2011) 4606–4609.

[16] C. C. Berry, G. Campbell, A. Spadiccino, M. Robertson, A. S. Curtis, The influence of microscale topography on fibroblast attachment and motility, Biomaterials 25 (26) (2004) 5781–5788.

[17] L. Pieuchot, J. Marteau, A. Guignandon, T. Dos Santos, I. Brigaud, P.-F. Chauvy, T. Cloatre, A. Ponche, T. Petithory, P. Rougerie, et al., Curvotaxis directs cell migration through cell-scale curvature landscapes, Nature Communications 9 (1) (2018) 1–13.

[18] M. Nikkhah, F. Edalat, S. Manoucheri, A. Khademhosseini, Engineering microscale topographies to control the cell–substrate interface, Biomaterials 33 (21) (2012) 5230–5246.

[19] H. N. Kim, A. Jiao, N. S. Hwang, M. S. Kim, D.-H. Kim, K.-Y. Suh, et al., Nanotopography-guided tissue engineering and regenerative medicine, Advanced Drug Delivery Reviews 65 (4) (2013) 536–558.

[20] H. Jeon, C. G. Simon Jr, G. Kim, A mini-review: cell response to microscale, nanoscale, and hierarchical patterning of surface structure,

Journal of Biomedical Materials Research Part B: Applied Biomaterials 102 (7) (2014) 1580–1594.

[21] H. N. Kim, Y. Hong, M. S. Kim, S. M. Kim, K.-Y. Suh, Effect of orientation and density of nanotopography in dermal wound healing, Biomaterials 33 (34) (2012) 8782–8792.

[22] H. Rostam, S. Singh, N. Vrana, M. Alexander, A. Ghaemmaghami, Impact of surface chemistry and topography on the function of antigen presenting cells, Biomaterials Science 3 (3) (2015) 424–441.

[23] R. J. Petrie, A. D. Doyle, K. M. Yamada, Random versus directionally persistent cell migration, Nature Reviews Molecular Cell Biology 10 (8) (2009) 538–549.

[24] J. Kim, Y. Cao, C. Eddy, Y. Deng, H. Levine, W.-J. Rappel, B. Sun, The mechanics and dynamics of cancer cells sensing noisy 3d contact guidance, Proceedings of the National Academy of Sciences 118 (10) (2021).

[25] C. Leclech, A. I. Barakat, Is there a universal mechanism of cell alignment in response to substrate topography?, Cytoskeleton 78 (6) (2021) 284–292.

[26] A. Ray, O. Lee, Z. Win, R. M. Edwards, P. W. Alford, D.-H. Kim, P. P. Provenzano, Anisotropic forces from spatially constrained focal adhesions mediate contact guidance directed cell migration, Nature Communications 8 (1) (2017) 1–17.

[27] D. W. Hamilton, S. Ghrebi, H. Kim, B. Chehroudi, D. M. Brunette, Surface topography and cell behaviour, in: Encyclopedia of Biomaterials and Biomedical Engineering, Taylor and Francis New York, 2006, pp. 1–15.

[28] P. Thomsen, C. Gretzer, Macrophage interactions with modified material surfaces, Current Opinion in Solid State and Materials Science 5 (2-3) (2001) 163–176.

[29] L. Ge, L. Yang, R. Bron, J. K. Burgess, P. van Rijn, Topography-mediated fibroblast cell migration is influenced by direction, wavelength, and amplitude, ACS Applied Bio Materials 3 (4) (2020) 2104–2116.

[30] C. Dai, S. Shih, A. Khachemoune, Skin substitutes for acute and chronic wound healing: an updated review, Journal of Dermatological Treatment 31 (6) (2020) 639–648.

[31] A. Curtis, M. Riehle, Tissue engineering: the biophysical background, Physics in Medicine & Biology 46 (4) (2001) R47.

[32] V. H. Barocas, R. T. Tranquillo, An anisotropic biphasic theory of tissue-equivalent mechanics: the interplay among cell traction, fibrillar network deformation, fibril alignment, and cell contact guidance, Journal of Biomechanical Engineering 119 (2) (1997) 137–145.

[33] J. C. Dallon, J. A. Sherratt, P. K. Maini, Mathematical modelling of extracellular matrix dynamics using discrete cells: fiber orientation and tissue regeneration, Journal of Theoretical Biology 199 (4) (1999) 449–471.

[34] S. McDougall, J. Dallon, J. Sherratt, P. Maini, Fibroblast migration and collagen deposition during dermal wound healing: mathematical modelling and clinical implications, Philosophical Transactions of the Royal Society A: Mathematical, Physical and Engineering Sciences 364 (1843) (2006) 1385–1405.

[35] T. Heydari, M. Heidari, O. Mashinchian, M. Wojcik, K. Xu, M. J. Dalby, M. Mahmoudi, M. R. Ejtehadi, Development of a virtual cell model to predict cell response to substrate topography, ACS Nano 11 (9) (2017) 9084–9092.

[36] B. Winkler, I. S. Aranson, F. Ziebert, Confinement and substrate topography control cell migration in a 3d computational model, Communications Physics 2 (1) (2019) 1–11.

[37] C. L. Stokes, D. A. Lauffenburger, S. K. Williams, Migration of individual microvessel endothelial cells: stochastic model and parameter measurement, Journal of Cell Science 99 (2) (1991) 419–430.

[38] M. Irving, M. F. Murphy, F. Lilley, P. W. French, D. R. Burton, S. Dixon, M. C. Sharp, The use of abrasive polishing and laser processing for developing polyurethane surfaces for controlling fibroblast cell behaviour, Materials Science and Engineering: C 71 (2017) 690–697.

[39] D. Conway, Integrating in-silico models with in-vitro data to generate novel insights into biological systems, Ph.D. thesis, Liverpool John Moores University (2019).

[40] G. Dunn, A. Brown, A unified approach to analysing cell motility, Journal of Cell Science 1987 (Supplement_8) (1987) 81–102.

[41] D. J. Higham, An algorithmic introduction to numerical simulation of stochastic differential equations, SIAM Review 43 (3) (2001) 525–546.